



Wide-viewing full-color depthmap computer-generated holograms

SUNGJAE PARK,¹ JONGHYUN LEE,¹  SUNGJIN LIM,² MUGEON KIM,² SUNGGYUN AHN,² SOONHYOUNG HWANG,³ SOHEE JEON,³ JUNHO JEONG,³ JOONKU HAHN,^{2,4} AND HWI KIM^{1,5}

¹*Department of Electronics and Information Engineering, College of Science and Technology, Korea University, Sejong-Campus, 2511 Sejong-ro, Sejong 30019, Republic of Korea*

²*School of Electronic and Electrical Engineering, Kyungpook National University, Buk-Gu, 80 Daehak-ro, Daegu 41566, Republic of Korea*

³*Nano-Convergence Mechanical Systems Research Division, Korea Institute of Machinery and Materials, Daejeon, 34103, Republic of Korea*

⁴*jhahn@knu.ac.kr*

⁵*hwikim@korea.ac.kr*

Abstract: An efficient synthesis algorithm for wide-viewing full-color depthmap computer-generated holograms is proposed. We develop a precise computational algorithm integrating wave-optic geometry-mapping, color-matching, and noise-filtering to multiplex multiview elementary computer-generated holograms (CGHs) into a single high-definition CGH without three-dimensional perspective distortion or color dispersion. Computational parallelism is exploited to achieve significant computational efficiency improvement in the production throughput of full-color wide-viewing angle CGHs. The proposed algorithm is verified through the full-color binary hologram reconstruction experiments utilizing an off-axis R-G-B simultaneous illumination method, which suggests the feasibility of the full-color sub-wavelength binary spatial light modulator technology.

© 2021 Optical Society of America under the terms of the [OSA Open Access Publishing Agreement](#)

1. Introduction

The technology for generating three-dimensional (3D) holographic images from computer-generated holograms (CGHs) has been extensively researched over recent decades. The key-factor for a holographic display is a spatial light modulator (SLM) with a small pixel pitch on the wavelength scale. Still, state-of-the-art SLMs have not yet reached the necessary technology level in terms of pixel pitch size and resolution. Research has been undertaken into overcoming such physical limitations in the development of holographic 3D displays through using dynamic light wave steering techniques and advancing SLM technology [1,2]. It is noteworthy that a liquid crystal-based SLM technology implementing a pixel pitch of 1 μm was announced recently [3].

Regarding the CGH theory, the binary modulation SLM design would be acceptable in practice. Although the binary CGH design has a physical limitation in the modulation of light field, it can generate high-quality CGH scenes, and only binary modulation in amplitude or phase may simplify the architecture design of SLM and enables the realization of SLM with sub-micro scale pixel size [4]. A few studies related to binary SLM technology have been reported. The binary SLM technologies using microelectromechanical system (MEMS) [5], phase change material [6], and related noise reduction techniques [7,8] are considerable research topics. Moreover, it is evident that advanced RGB color filters need to be applied to all small unit pixels of CGH to represent full-color holographic images under white-light illumination. The hybridization of recent advanced single-pixel structural color filter technology and spatial light modulation technology will be a promising candidate that realizes full-color CGH on the deep-subwavelength binary pattern. However, from a practical point of view, we can suppose

the off-axis RGB illumination method [9,10] practically acceptable when we employ the RGB simultaneous-illumination for binary holographic display.

Static CGHs are also used to validate the feasibility of a three-dimensional (3D) holographic display featuring a wide-viewing angle, large viewing-zone (eye-motion box), and perfect accommodation effect [11,12]. Static CGHs with sub-wavelength-scale pixel pitch was demonstrated for full-color wide-viewing holographic image generation [13]. The metasurface platform is attractive as a promising CGH platform [14–16], and the rapid advances in CGH photopolymer printing technology allow us to expect the forthcoming arrival of portable CGH printers. The complex modulation architecture derived from the recent development of subwavelength photonics technology such as meta-surface and plasmonics is a strong candidate of SLM that guarantees to enhance the light field modulation range of CGH [17]. Full-color holograms can be implemented with stripe pattern color filters [18] or by stacking multiple holograms [13] as well as off-axis RGB illumination method [9,10].

Meanwhile, challenges remain in the computational CGH synthesis algorithm. The creation of photorealistic holographic 3D scenes using a fast algorithm is the main research focus. CGH synthesis algorithms have generally been classified according to the representation model of the object and optical field into four types, the point cloud, triangular mesh, light-field, and depth-map modes. In this paper, large-scale wide-viewing angle CGH is of principal interest. The substantial amount of wave-optic information in wide-view 3D scenes necessitates a more efficient numerical scheme. A few previous research works have been devoted to large-scale wide-viewing CGHs. The traditional point cloud method expresses an object's surface by many points [19,20]. Since the interference pattern must be calculated for each point, the amount of calculation increases considerably. This issue has been more efficiently dealt with in the CGH synthesis methods based on polygon model [13,18,21] and light-field conversion [22,23] model. The polygon method calculates the diffraction pattern of each object surface expressed as a polygonal mesh. The advantage of the polygon and light-field methods is their accurate representation of 3D objects. However, they tend to become time-consuming as target object complexity increases. The computational efficiency is linked with object complexity, and the computational time cannot be quantified and remains cumbersome when applied to general complex objects or scenes. The light-field conversion method is advantageous for photorealistic CGH synthesis, and its computation can be accelerated using a graphics processing unit (GPU) [23]. The depth-map CGH synthesis method based on the layered-object model calculates CGHs using the fast Fourier transform (FFT) [12,24]. The number of model layers determines its calculation amount. When creating a full-color CGH, the wavelength-dependent diffraction characteristics need to be very carefully accounted for. Still, in the depthmap CGH synthesis scheme, full-color CGH synthesis is efficiently processed [24–29], and this advantage of the depth-map calculation method becomes a key consideration when implementing CGHs requiring a large amount of computation, such as full-color wide-viewing angle CGHs. Recently, deep-learning technique was successfully used for the real-time processing of the depthmap CGH [30].

This paper proposes a depthmap-based, full-color wide-viewing angle hologram synthesis scheme and verifies it through numerical simulation and experiment. In particular, the possibility of the full color wide-viewing binary CGH is investigated in the experiment, which can be a practical model for dynamic full-color wide-viewing angle holographic 3D display. In section 2, the proposed wide-viewing depthmap CGH synthesis algorithm is described step-by-step. In section 3, the experimental verification of the proposed method is presented by optical CGH reconstruction, and in section 4, concluding remarks are given.

2. Depthmap CGH synthesis algorithm

Here, the proposed design scheme of the wide viewing angle full color depthmap CGH is described, which consists of the elements: wave-optic geometry-mapping, color-matching, and

noise filtering steps. For the parallel calculation of CGH, a segmentation or partitioning that enables independent calculation of partial CGH components is designed. In the polygon CGH design, spatial division in the object plane is used, as depicted in Fig. 1(a). The local CGH pattern of a single polygon unit is taken locally, and the total CGH pattern is synthesized by superposition of every partial CGH pattern in the total CGH plane ($z=0$). The object plane's spatial segmentation was proven to produce high-quality holographic 3D images and secures computational parallelism for the polygon CGH. However, it is not appropriate for wide-viewing depthmap CGH synthesis since standard depthmap data does not use object segmentation in the xy plane but z -directional sectioning. Depthmap CGH allows us to approximate photorealistic scenes using a limited number of image data depths, providing excellent flexibility for the large-scale CGHs. This paper proposes a simple and efficient viewing zone partitioning method for wide-viewing angle depthmap CGH that enables desirable, efficient parallel computation (Fig. 1(b)). The object domain segmentation method and viewing-zone partitioning method are compared in Figs. 1(a) and 1(b).

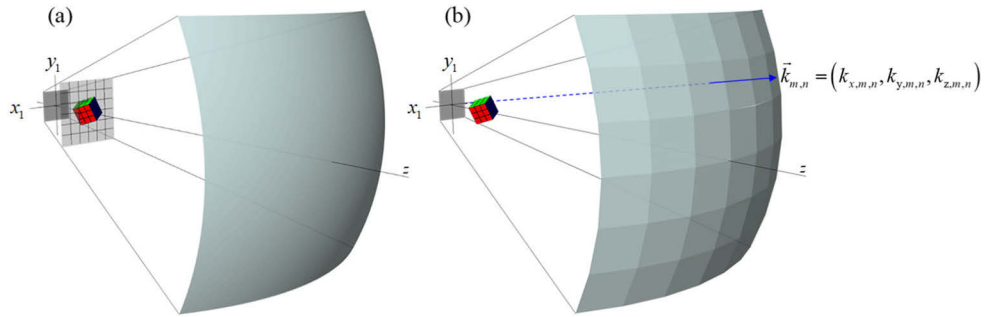


Fig. 1. Two approaches for wide-viewing-angle CGH parallel computation : (a) Object domain segmentation and (b) viewing-zone partitioning

The proposed depthmap CGH computation is composed of two steps. The first step computes the (m, n) partial CGH $F_{m,n}(x_1, y_1)$ with $M \times N$ resolution. The second collects and multiplexes all components $F_{m,n}(x_1, y_1)$ with the corresponding carrier wave $\exp(j(k_{m,n,x}x_1 + k_{m,n,y}y_1))$ in the total CGH plane ($z = 0$), which is the lateral component of the carrier wave $\exp(j(k_{m,n,x}x + k_{m,n,y}y + k_{m,n,z}z))$. This step multiplies the carrier wave to the partial CGH along each direction and combines them to a single CGH plane. The resulting total CGH is represented as

$$total_CGH = \sum_m \sum_n \exp(j(k_{m,n,x}x_1 + k_{m,n,y}y_1))F_{m,n}(x_1, y_1), \quad (1)$$

where the lateral k-vector $(k_{m,n,x}, k_{m,n,y})$ is given by

$$(k_{m,n,x}, k_{m,n,y}) = \frac{2\pi}{\lambda} (\cos \phi_{m,n} \sin \theta_{m,n}, \sin \phi_{m,n} \sin \theta_{m,n}). \quad (2)$$

The carrier wave component plays the role of delivering the holographic image signal to the (m, n) th viewing zone. In the schematic of Fig. 1(b), the angular diffraction field $F_{m,n}(x_1, y_1)$ is distributed on the (m, n) th viewing zone, where the viewer's eye is placed and perceives 3D holographic image. For each single directional elementary CGH, we use the depthmap CGH synthesis algorithm developed in our previous research [24,25]. For the computation of $F_{m,n}(x_1, y_1)$, the complex field $W_{m,n}(x'_1, y'_1)$ is first calculated at the $x'_1 y'_1$ plane orthogonal to the off-axis viewing direction. Next, the field mapping process is performed to determine the complex field distribution on the $x_1 y_1$ plane, $F_{m,n}(x_1, y_1)$.

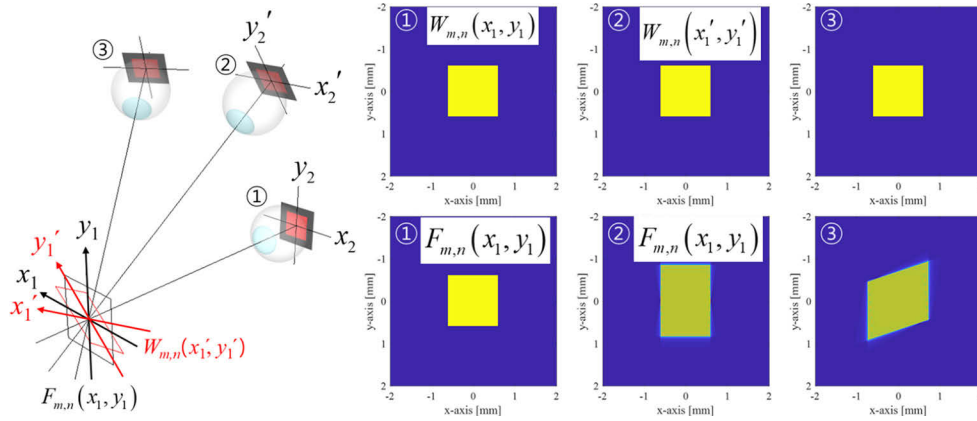


Fig. 3. Concept of the field mapping algorithm: comparison of the variations in $F_{m,n}(x_1, y_1)$ for on-axis and off-axis positions. $W_{m,n}(x'_1, y'_1)$ is set to the same rectangular field distribution.

$W_{m,n}(x_1, y_1, 0)$ is represented by

$$\begin{aligned}
 W_{m,n}(x_1, y_1, 0) &= \eta_0 e^{j2\pi(\alpha_{m,n}x_1 + \beta_{m,n}y_1)} \iint \left[A_{m,n}(\alpha'(\alpha + \alpha_{m,n}, \beta + \beta_{m,n}), \beta'(\alpha + \alpha_{m,n}, \beta + \beta_{m,n})) \right. \\
 &\quad \left. \times \left| \cos \theta_{m,n} + \frac{\sin \theta_{m,n}(\cos \phi_{m,n}(\alpha + \alpha_{m,n}) + \sin \phi_{m,n}(\beta + \beta_{m,n}))}{\gamma(\alpha + \alpha_{m,n}, \beta + \beta_{m,n})} \right| \right] e^{j2\pi(\alpha x_1 + \beta y_1)} d\alpha d\beta \\
 &= \eta_0 e^{j2\pi(\alpha_{m,n}x_1 + \beta_{m,n}y_1)} \iint \bar{A}_{m,n}(\alpha, \beta) e^{j2\pi(\alpha x_1 + \beta y_1)} d\alpha d\beta \\
 &= \eta_0 e^{j2\pi(\alpha_{m,n}x_1 + \beta_{m,n}y_1)} F_{m,n}(x_1, y_1),
 \end{aligned} \tag{5}$$

where $\bar{A}_{m,n}(\alpha, \beta)$ is the angular spectrum of the low-bandwidth holographic image (for the complete derivation, see Appendix). The light field distribution $F_{m,n}(x_1, y_1)$ in the global coordinate system can be extracted from $W_{m,n}(x_1, y_1, 0)$, which is the global coordinate version of $W_{m,n}(x'_1, y'_1, z'_1)$. It can be decomposed by the carrier wave term $e^{j2\pi(\alpha_{m,n}x_1 + \beta_{m,n}y_1)}$ and the low-bandwidth holographic image signal $F_{m,n}(x_1, y_1)$. $F_{m,n}(x_1, y_1)$ is interpreted as the low-bandwidth holographic image delivered to the (m,n)th viewing zone by the carrier frequency $e^{j2\pi(\alpha_{m,n}x_1 + \beta_{m,n}y_1)}$.

The important thing is that in the depthmap CGH computation, to achieve computational efficiency, we decompose Eq. (5) into the analytic carrier wave (for which dense sampling is needed) and the numerical partial CGH field (low-resolution). In the numerical computation of the total CGH of Eq. (1), the CGH component $W_{m,n}(x_1, y_1)$ should be sufficiently oversampled to secure the wave feature $e^{j2\pi(\alpha_{m,n}x_1 + \beta_{m,n}y_1)}$. For example, the resolution of $W_{m,n}(x_1, y_1)$ should be 30001×30001 for a corresponding $F_{m,n}(x_1, y_1)$ with resolution of just 2001×2001 .

2.2. Full-color depthmap computer-generated holograms

The advantage of the depthmap CGH is that computational complexity is object complexity invariant, so it has no limitations for representing complicated or photorealistic scenes. Thus, for depthmap CGHs, parallel computation is well defined, and enables the computational acceleration easily in the depthmap CGH.

As illustrated in Figs. 4(a) and (b), the depthmap CGH is calculated using several layers of the 3D object ($L_1 \sim L_n$) on the regular intervals of the optical axis. The input data of $L_1 \sim L_n$ is composed of the intensity image and depth data of the target object. Using the ICdFr algorithm [24], the depth-map CGH, $F_{m,n}(x_1, y_1)$, is obtained and is multiplexed to the total CGH by the form $W_{m,n}(x_1, y_1)$ (Eq. (1)). Because wide-viewing angle CGHs should allow observation of the

target object even on the off-axis, the object input data for each direction should be a sectionized image of the layered object as shown in Fig. 4(b). As represented in Fig. 4(c), a depthmap model of the target object is constructed for a specific viewing direction. Since the retinal plane's computational grid is independent of color in the depth-map CGH method, the algorithm allows the color matching of the R/G/B CGH components without an additional compensation algorithm [24]. The total CGH of Eq. (1) provides the viewer a wide-viewing angle 3D object from various directions with continuous parallax and full accommodation effect as shown in Fig. 4(d). Figure 5 presents the simulation result of the wide-viewing single color depthmap CGH, which shows that five different perspective views are reconstructed according to the viewing zone's observation position. The size of the CGH is about 2 cm by 2 cm, the pixel pitch is 0.425 μ m, and the wavelength is 488 nm blue. The simulation result confirms that the target object is well represented in various directions, and that the motion parallax phenomenon is well represented.

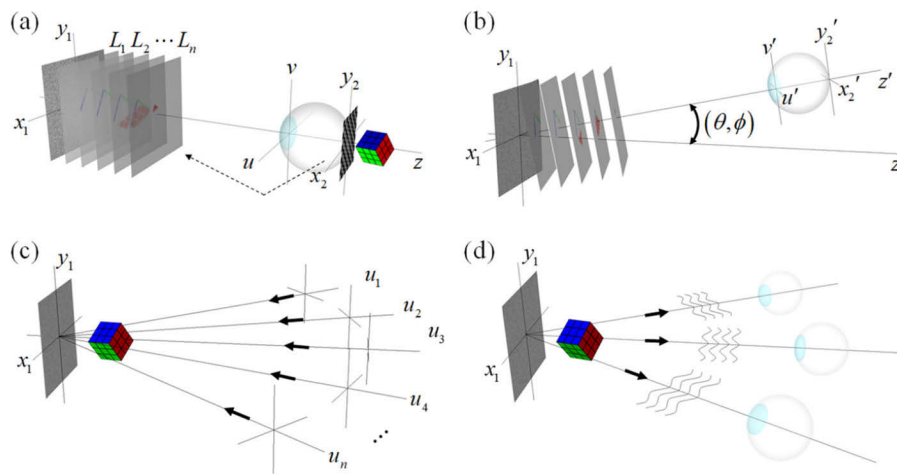


Fig. 4. Depth-map model of a 3D object for (a) normal viewing direction and (b) oblique viewing direction. (c) Angular multiplexing of angularly separated CGH field onto a single wide-viewing angle CGH plane (d) Observation of wide-viewing angle CGH. Field distribution of eye lens plane and reconstructed images of retina plane with wide-viewing single color depthmap CGH.

Regarding RGB color matching, two core algorithms have been developed to produce correctly-*RGB*-matched wide-viewing angle CGH 3D images. The primary consideration is that viewing zone size varies with *RGB* wavelengths, as indicated in Fig. 6(a). The blue wavelength, which is the shortest, generates a slightly smaller rectangular viewing zone than the green and red wavelengths. Therefore, if each *RGB* viewing zone is divided into 27 \times 27, the red, green, and blue subdivision units don't match each other. For example, a distorted image is observed because the (1,1) viewing window has a different position for each color as seen in Fig. 6. Figure 7 shows the field distribution of the eye lens plane and the retinal plane reconstructed image for the traditional full-color CGH calculated for *R*, *G*, and *B* wavelengths without any special compensating technique. Using the conventional method, the size of the signal field distribution on the eye lens plane (viewing zone) is expressed differently for *R*, *G*, and *B* wavelengths.

As a result, as shown in Fig. 7(d), on the full-color eye lens plane, the subdivision units of each color do not correspond well, resulting in a color mismatch problem. Reconstructed images showing the presentation of this phenomenon on the retinal plane are given in Fig. 7(e)-(g). At the center of the eye lens plane, each color's signals are matched, resulting in accurate full-color results even in the reconstructed image. On the other hand, on the periphery, the field distributions

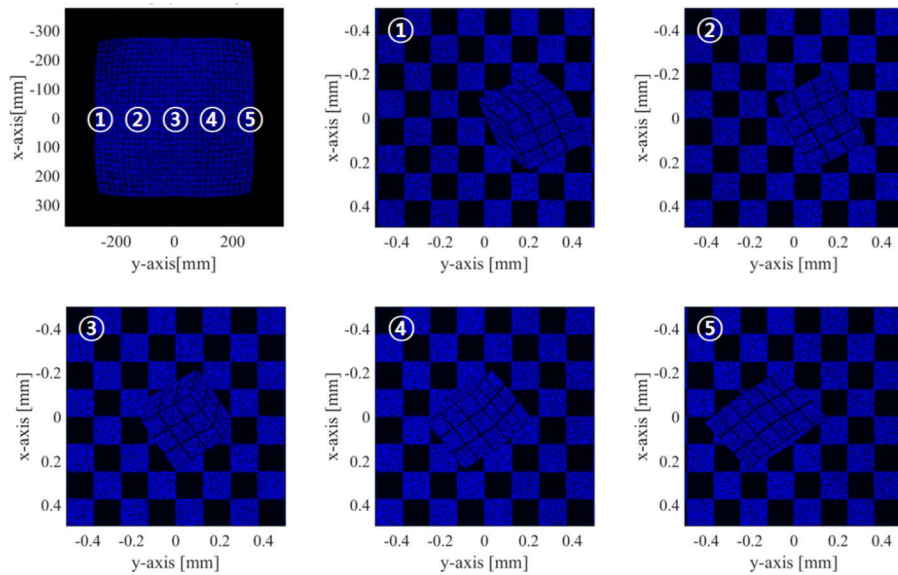


Fig. 5. Observation of wide-viewing angle CGH. Field distribution of the viewing zone plane and reconstructed images in the retina plane.

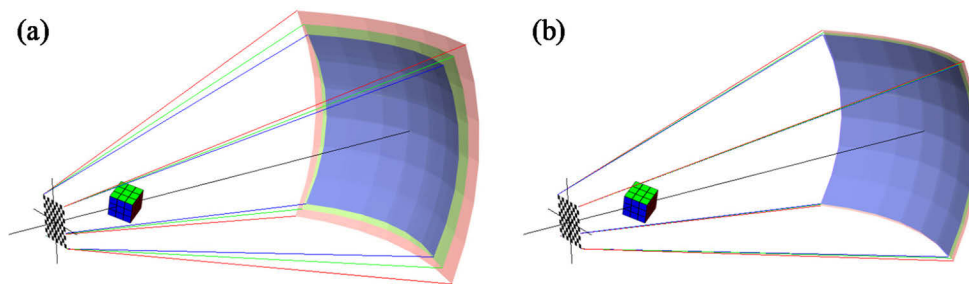


Fig. 6. (a) Traditional viewing zone for R, G, and B wavelengths, (b) Viewing zone for R, G, and B wavelength using the color-matching method.

of each color are poorly matched, so color mismatch problem appears as indicated by the red circles on the reconstructed images.

On the other hand, to accurately represent full-color in the eye lens plane, it is necessary to accord the size of the blue image, which has the shortest wavelength, so as to match the subdivision unit of each color. The main idea of the color matching method presented in Fig. 6(b) is simple; the size of the eye lens plane is set to the same size as the blue zone for all colors, and the RGB partial CGHs are calculated at the blue wavelength subdivision viewing zones, as shown in Figs. 8(a)-(d). Then, the color mismatch phenomenon does not appear in the full-color viewing window, as shown in Figs. 8(d)-(g). Using the color matching method, the signal distributions of R, G, and B wavelengths on the eye lens plane of the full-color CGH are expressed as in the same size, so the subdivision unit signals match at all positions on the eye lens plane. Therefore, as shown in Figs. 8(e)-(f), accurate full-color objects can be expressed at side positions in addition to the center position of the viewing window. In Figs. 7 and 8, full complex CGH is used to make it easier to understand the color matching method.

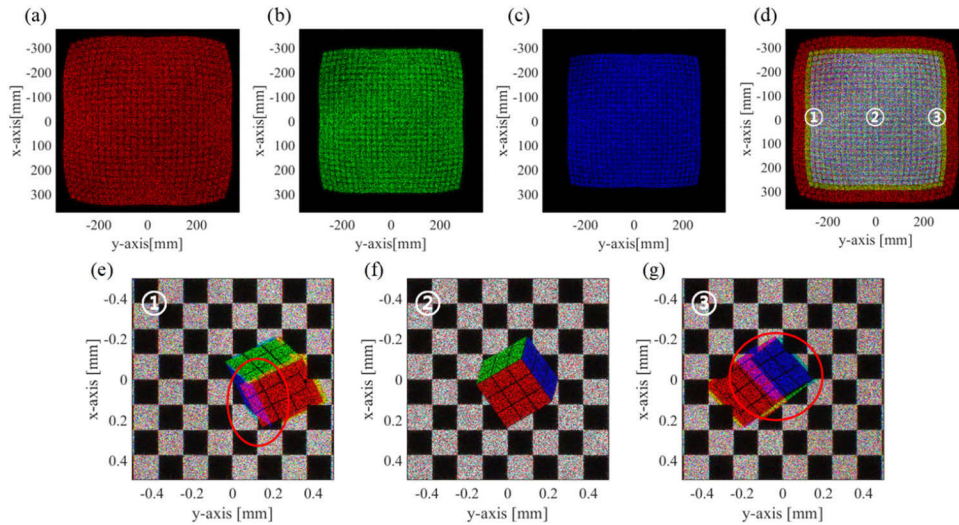


Fig. 7. Signal field distributions of (a) red, (b) green, (c) blue, (d) full-color in the eye lens plane for traditional full-color CGH, Reconstructed image on the retinal plane from the (e) left, (f) center, and (g) right sides.

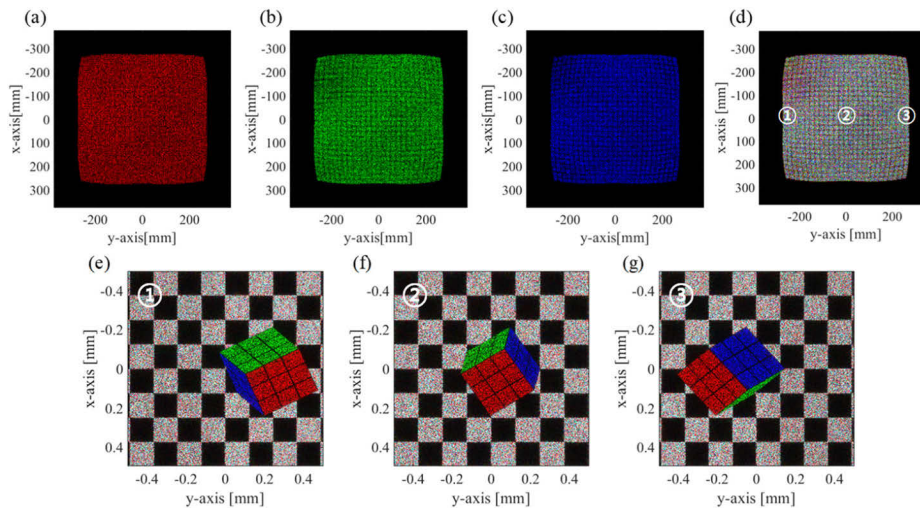


Fig. 8. Signal field distribution of (a) red, (b) green, (c) blue, (d) full-color in the eye lens plane for full-color CGH using the color matching method, Reconstructed image on the retinal plane from the (e) left, (f) center, and (g) right sides.

2.3. Noise filter for improving image quality

Even though the total viewing zone area is fitted to the viewing zone of the shorted blue wavelength, each elementary viewing zone size is different for R, G, and B wavelengths, as shown in Fig. 9(a). In the depth map CGH synthesis, the R and G subdivision components overlap their neighbor subdivision units. In practice, this overlap induces an erroneous holographic image when the viewer's eye is placed on the overlapping area in the viewing zone. Thus, filtering the R and G components to trim the over-sized parts and fit them into the blue viewing zone's exact size is necessary. Let us refer to this filtering technique by B-zone filtering. Figure 9

compares the holographic image synthesis results both with and without B-zone filtering of R and G components. It is seen that double image deterioration is observed in the former case, while after filtering, in the latter, the double image deterioration is removed.

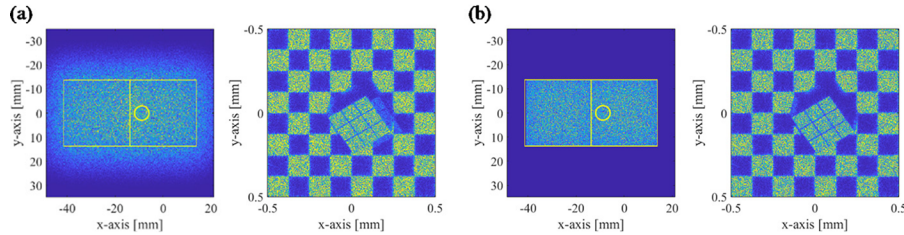


Fig. 9. Holographic images reconstructed (a) without B-zone filtering and (b) with B-zone filtering.

Regarding computational efficiency, the filtering and noise reduction process is the most time-consuming. Common sense suggests that the computational burden is mainly imposed by the CGH pattern calculation. However, our observation is that in practice more effort to accelerate the filtering process should be made. The filtering process is heavy in terms of computation because $M \times N$ individual CGHs are located in the CGH plane, and, to use the filtering method, they should be sent to the eye-lens plane through the inverse Fresnel transform [23]. The field distribution to which the filtering method has been applied should then be sent back to the CGH plane through the forward Fresnel transform. In this process, each CGH filtering process is performed for $W_{m,n}(x_1, y_1)$ with the full-resolution of the total CGH included, making the calculation intensive. This issue will be further improved by continuing research. To sum up, the CGH synthesis algorithm has three core elements: (i) angular multiplexing of viewing zone subdivision CGH components, (ii) viewing zone design, and (iii) filtering of the R and G components, in which the viewing zone and subdivision areas of the R and G components are tailored to fit to the B component dimension. As a result, the viewing zone and viewing angle of the CGH are constraint by the B-viewing zone.

3. Experimental results

For the experimental verification of the proposed CGH design method, we adopt the RGB off-axis illumination setup illustrated in Fig. 10. The CGH pattern used in this test is a binary pattern fabricated in the form of a binary mask pattern [21]. The binary design generates DC and conjugate noises in the viewing zone. The signal, DC, and conjugate component distribution of the RGB wavelengths are formed in the viewing zone, as shown in Fig. 10. Three R-G-B laser beams with their own oblique incidence angles illuminate the CGH leading to the spatial shift of the diffraction fields in the eye lens plane. The red laser beam with a downward obliqueness adjusts the trigonal pyramid to the center of the eye-lens plane, the green beam with on-axis non-obliqueness tunes the green sphere, and the blue beam with an upward obliqueness locates the lower blue rectangular parallelepiped to the exact center of the eye-lens plane. Under simultaneous illumination of the three R-G-B lasers, the viewer can see the red pyramid, green sphere, and blue parallelepiped simultaneously through the overlapped viewing zone of the three R-G-B viewing zones, which is referred to as the region of interest (ROI) (Fig. 10). This means that an accurate full-color holographic image can be observed in the ROI. Roughly the ROI region is about 1/3 the area of the total viewing zone. The precise alignment of RGB beams and optimal RGB CGH component design is necessary. This method has the disadvantage of using about 1/3 of the viewing zone in the vertical direction, but all of the horizontal direction's viewing angles are maintained.

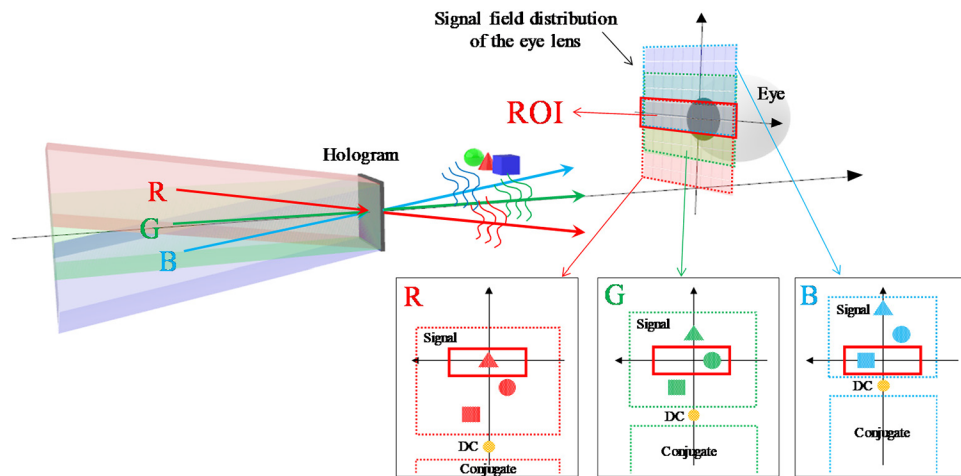


Fig. 10. Schematic of wide-viewing full-color CGH using the off-axis illumination method

In Fig. 11, the experimental setup for observing the wide-viewing full-color CGH is presented. R(638 nm), G(532 nm), and B(488 nm) laser beams are collimated by the 300 mm focal length lens to form an expanded plane wave. Each collimated wave is tuned by mirrors to impinge on the binary CGH sample with the specific oblique incidence angle according to wavelength. Here, the R-G-B beam incident angles on the CGH are set to 9° , 0° , and 6° , respectively. The perspective view of the CGH is measured by changing the viewing angle of the charge coupled device (CCD) camera mounted on the rotation stage. The viewing distance of the CCD from the CGH is set to 1 m. The implemented experimental setup is shown in Fig. 11(b).

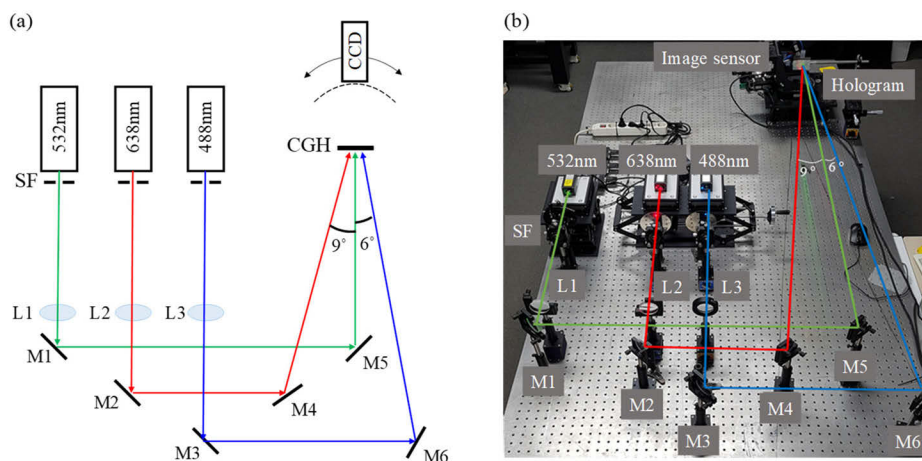


Fig. 11. (a) System configuration and (b) experiment setup to observe wide-viewing full-color CGH using the off-axis illumination method. SF, spatial filter; L1-L3, collimation lens; M1-M6, mirrors. The incidence angles of R (638 nm), G (532 nm), and B (488 nm) laser beams on the CGH sample are 9° , 0° , and 6° , respectively.

A Rubik's cube and checkerboard at different depth positions are used as the objects of the CGH, as shown in Fig. 2. The size, resolution, and pixel pitch of the fabricated CGH sample in the experiment are $20\text{mm} \times 20\text{mm}$, 46899×46899 , and 425nm , respectively. The signal field distribution in the eye-lens plane and the reconstructed image on the retinal plane of the

wide-viewing full-color CGH are presented with respect to viewing angle in Figs. 12(a)–12(d). This full-color CGH is estimated to have a horizontal viewing angle of 70 degrees and a vertical viewing angle of 35 degrees. Figures 12(e)–12(g) present the experimental observation of the binary CGH sample taken by the CCD with the viewing angle of observation ranged from -35° to $+35^\circ$. The experimental results show good agreement with the simulation results also in Fig. 12. We see that the CGH design method is capable of representing a holographic 3D image with a wide-viewing angle and accurate colors. The parameters applied to the simulation and experiment are summarized in Table 1.

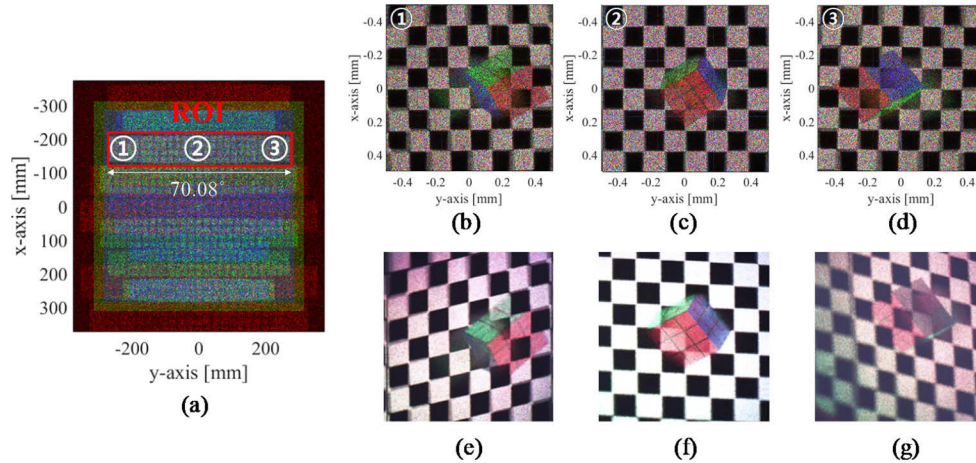


Fig. 12. Wide-viewing full-color binary CGH; comparison of simulation and experimental results. Simulation results of (a) signal field distribution of the eye lens plane, (b-d) reconstructed images in the retinal plane according to viewing angle (-35° , 0° , $+35^\circ$). (e-g) Observation experimental results depending on viewing angle (-35° , 0° , $+35^\circ$). (See [Visualization 1](#) and [Visualization 2](#))

Table 1. System specifications & design parameters of the fabricated CGH

Sample size	20mm x 20mm	Object size (Cube/Checkboard)	10mm x 10mm / 20mm x 20mm
Pixel pitch	425nm		
Resolution	46899x 46899	Incident angle (R/G/B)	$9^\circ / 0^\circ / 6^\circ$
Wavelength (R/G/B)	638nm/532nm/488nm		

4. Conclusion

In conclusion, we proposed the design method for wide-viewing full-color depthmap CGHs based on the viewing-zone partitioning and verified its feasibility experimentally. The design process consists of the multi-steps of field-mapping, color-matching, noise filtering, and integrable multiplexing of partial CGHs into a single high-definition CGH. It has been shown that this stepwise process produces a wide-viewing angle full-color CGH pattern without 3D perspective distortion and color dispersion. We believe the static CGH experiment in this paper supports the feasibility and future research direction of wide-viewing angle full-color CGH using the binary SLM technology with the RGB simultaneous-illumination.

Appendix: Partial CGH component for the (m,n)th viewing zone

We provide the detailed mathematical formulation of the field mapping theory in section 2.1. As seen in Fig. 13, the total CGH delivers the (m,n)th directional depthmap holographic image signal to the (m,n)th viewing zone. Fig. 13 presents a schematic of the local and global grid for the oblique viewing direction and the reconstructed images from each axis. Naturally, the correct square image on the tilted optical axis (local axis) is distorted on the global axis.

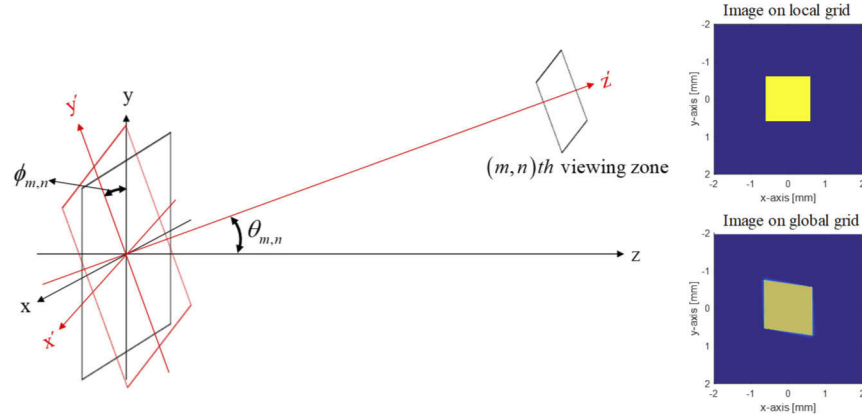


Fig. 13. Schematic and reconstructed images of local and global axes for the (m,n)th viewing zone

In the synthesis of the total CGH, the partial CGH for the (m,n)th viewing zone $F_{m,n}(x, y)$ is multiplexed at the CGH plane ($z = 0$) by the carrier wave $\eta_0 \exp(j2\pi(\alpha_{m,n}x + \beta_{m,n}y))$. The total CGH is obtained by the superposition of all the partial CGH components as

$$total_CGH = \sum_m \sum_n \exp(j2\pi(\alpha_{m,n}x + \beta_{m,n}y)) F_{m,n}(x, y). \quad (S1)$$

where the spatial frequency is $(\alpha_{m,n}, \beta_{m,n}) = (1/\lambda)(\sin \theta_{m,n} \cos \phi_{m,n}, \sin \theta_{m,n} \sin \phi_{m,n})$, and $\theta_{m,n}$ and $\phi_{m,n}$ are the longitudinal angle and azimuthal angle, respectively.

To synthesize the geometrically corrected partial CGH $F_{m,n}(x, y)$ at $z = 0$, we should find it from the local CGH field distribution at the tilted plane $x'y'$. The local coordinate (x', y', z') is related to the global coordinate (x, y, z) through the Global to Local (GtoL) matrix transformation. The GtoL matrix transformation is defined by

$$\begin{pmatrix} x' \\ y' \\ z' \end{pmatrix} = \begin{pmatrix} \cos \tau \cos \theta \cos \phi - \sin \tau \sin \phi & \cos \tau \cos \theta \sin \phi + \sin \tau \cos \phi & -\cos \tau \sin \theta \\ -\sin \tau \cos \theta \cos \phi - \cos \tau \sin \phi & -\sin \tau \cos \theta \sin \phi + \cos \tau \cos \phi & \sin \tau \sin \theta \\ \sin \theta \cos \phi & \sin \theta \sin \phi & \cos \theta \end{pmatrix} \begin{pmatrix} x \\ y \\ z \end{pmatrix}. \quad (S2)$$

where $\theta_{m,n}$ and $\phi_{m,n}$ are denoted by θ and ϕ for simplicity, and τ is the rotation angle. Similarly, the relationship between the spatial frequencies in the local and global coordinate systems is given by

$$\begin{pmatrix} \alpha' \\ \beta' \\ \gamma' \end{pmatrix} = GtoL \begin{pmatrix} \alpha \\ \beta \\ \gamma \end{pmatrix}. \quad (S3)$$

The spatial frequency components in the local coordinate system, $\alpha'(\alpha, \beta)$, $\beta'(\alpha, \beta)$ and $\gamma'(\alpha, \beta)$, are solved through α , β , and γ in the global coordinate system;

$$\alpha'(\alpha, \beta) = (\cos \tau \cos \theta \cos \phi - \sin \tau \sin \phi)\alpha + (\cos \tau \cos \theta \sin \phi + \sin \tau \cos \phi)\beta - \cos \tau \sin \theta \gamma, \quad (\text{S4})$$

$$\beta'(\alpha, \beta) = (-\sin \tau \cos \theta \cos \phi - \cos \tau \sin \phi)\alpha + (-\sin \tau \cos \theta \sin \phi + \cos \tau \cos \phi)\beta + \sin \tau \sin \theta \gamma, \quad (\text{S5})$$

$$\gamma'(\alpha, \beta) = \sin \theta \cos \phi \alpha + \sin \theta \sin \phi \beta + \cos \theta \gamma. \quad (\text{S6})$$

Let the CGH field at the local $x'y'$ plane be represented by the angular spectrum integral by

$$W_{m,n}(x', y', 0) = \eta_0 \iint A_{m,n}(\alpha', \beta') \exp(j2\pi(\alpha'x' + \beta'y')) d\alpha' d\beta'. \quad (\text{S7})$$

Then, the light field distribution representation of the local coordinate system is extended to

$$W_{m,n}(x', y', z') = \eta_0 \iint A_{m,n}(\alpha', \beta') \exp(j2\pi(\alpha'x' + \beta'y' + \gamma'z')) d\alpha' d\beta'. \quad (\text{S8})$$

By substituting Eqs. (S2) and (S3) into Eq. (S7) and using the invariance $\alpha x + \beta y + \gamma z = \alpha'x' + \beta'y' + \gamma'z'$ for the GtoL transformation, we obtain the light field distribution $W_{m,n}(x, y, z)$ in the global coordinate as Eq. (S9),

$$W_{m,n}(x, y, z) = \eta_0 \iint \left[A_{m,n}(\alpha'(\alpha, \beta), \beta'(\alpha, \beta)) \left| \cos \theta + \frac{\sin \theta (\cos \phi \alpha + \sin \phi \beta)}{\gamma} \right| \right] e^{j2\pi(\alpha x + \beta y + \gamma z)} d\alpha d\beta. \quad (\text{S9})$$

Before manifesting the Jacobian determinant $|\cos \theta + \sin \theta (\cos \phi \alpha + \sin \phi \beta) / \gamma|$, let us see the field distribution $W_{m,n}(x, y, 0)$. In $W_{m,n}(x, y, 0)$, the carrier wave term $\eta_0 \exp(j2\pi(\alpha_{m,n}x + \beta_{m,n}y))$ is separable from the low-frequency partial CGH term $F_{m,n}(x, y)$ as follows:

$$\begin{aligned} W_{m,n}(x, y, 0) &= \eta_0 \iint \left[\begin{array}{l} A_{m,n}(\alpha'(\alpha, \beta), \beta'(\alpha, \beta)) \\ \left| \cos \theta_{m,n} + \frac{\sin \theta_{m,n} (\cos \phi_{m,n} \alpha + \sin \phi_{m,n} \beta)}{\gamma} \right| \end{array} \right] \times \exp(j2\pi(\alpha x + \beta y)) d\alpha d\beta \\ &= \eta_0 e^{j2\pi(\alpha_{m,n}x + \beta_{m,n}y)} F_{m,n}(x, y). \end{aligned} \quad (\text{S10})$$

As a consequence, we find the angular spectrum of $F_{m,n}(x, y)$

$$F_{m,n}(x, y) = \iint \bar{A}(\alpha, \beta) e^{j2\pi(\alpha x + \beta y)} \alpha d\beta. \quad (\text{S11})$$

where the angular spectrum $\bar{A}(\alpha, \beta)$ is given by

$$\bar{A}(\alpha, \beta) = A_{m,n}(\alpha'(\alpha + \alpha_{m,n}, \beta + \beta_{m,n}), \beta'(\alpha + \alpha_{m,n}, \beta + \beta_{m,n})) \left| \cos \theta_{m,n} + \frac{\sin \theta_{m,n} (\cos \phi_{m,n} (\alpha + \alpha_{m,n}) + \sin \phi_{m,n} (\beta + \beta_{m,n}))}{\gamma(\alpha + \alpha_{m,n}, \beta + \beta_{m,n})} \right|. \quad (\text{A9b})$$

where $A_{m,n}(\alpha'(\alpha, \beta), \beta'(\alpha, \beta))$ is the mapping of $A_{m,n}$ from the local coordinate (α', β') to the global coordinate (α, β) . In practice, this numerical mapping can be calculated by using MATLAB built-in function GriddedInterpolant.

Next, let us discuss about the Jacobian determinant related to the variable change between (α', β') and (α, β) . The relationship between $\begin{pmatrix} d\alpha'(\alpha, \beta) \\ d\beta'(\alpha, \beta) \end{pmatrix}$ and $\begin{pmatrix} d\alpha \\ d\beta \end{pmatrix}$ is represented by

$$\begin{pmatrix} d\alpha'(\alpha, \beta) \\ d\beta'(\alpha, \beta) \end{pmatrix} = \begin{pmatrix} \frac{\partial\alpha'(\alpha, \beta)}{\partial\alpha} & \frac{\partial\alpha'(\alpha, \beta)}{\partial\beta} \\ \frac{\partial\beta'(\alpha, \beta)}{\partial\alpha} & \frac{\partial\beta'(\alpha, \beta)}{\partial\beta} \end{pmatrix} \begin{pmatrix} d\alpha \\ d\beta \end{pmatrix} = \begin{pmatrix} A & B \\ C & D \end{pmatrix} \begin{pmatrix} d\alpha \\ d\beta \end{pmatrix}. \quad (\text{S12})$$

where A , B , C , and D are derived from Eqs. (S4)-(S6) and given by

$$A = \frac{\partial\alpha'(\alpha, \beta)}{\partial\alpha} = \cos\tau \cos\theta \cos\phi - \sin\tau \sin\phi + \frac{\alpha \cos\tau \sin\theta}{\gamma}, \quad (\text{S13})$$

$$B = \frac{\partial\alpha'(\alpha, \beta)}{\partial\beta} = \cos\tau \cos\theta \sin\phi + \sin\tau \cos\phi + \frac{\beta \cos\tau \sin\theta}{\gamma}, \quad (\text{S14})$$

$$C = \frac{\partial\beta'(\alpha, \beta)}{\partial\alpha} = -\sin\tau \cos\theta \cos\phi - \cos\tau \sin\phi - \frac{\alpha \sin\tau \sin\theta}{\gamma}, \quad (\text{S15})$$

$$D = \frac{\partial\beta'(\alpha, \beta)}{\partial\beta} = -\sin\tau \cos\theta \sin\phi + \cos\tau \cos\phi - \frac{\beta \sin\tau \sin\theta}{\gamma}. \quad (\text{S16})$$

The Jacobian matrix is obtained as

$$\begin{pmatrix} d\alpha'(\alpha, \beta) \\ d\beta'(\alpha, \beta) \end{pmatrix} = \begin{pmatrix} \cos\tau \cos\theta \cos\phi - \sin\tau \sin\phi + \frac{\alpha \cos\tau \sin\theta}{\gamma} & \cos\tau \cos\theta \sin\phi + \sin\tau \cos\phi + \frac{\beta \cos\tau \sin\theta}{\gamma} \\ -\sin\tau \cos\theta \cos\phi - \cos\tau \sin\phi - \frac{\alpha \sin\tau \sin\theta}{\gamma} & -\sin\tau \cos\theta \sin\phi + \cos\tau \cos\phi - \frac{\beta \sin\tau \sin\theta}{\gamma} \end{pmatrix} \begin{pmatrix} d\alpha \\ d\beta \end{pmatrix}. \quad (\text{S17})$$

The determinant of the Jacobian matrix is shown in Eq. (S18);

$$d\alpha'(\alpha, \beta)d\beta'(\alpha, \beta) = \left| \cos\theta + \frac{\sin\theta(\alpha \cos\phi + \beta \sin\phi)}{\gamma} \right| d\alpha d\beta. \quad (\text{S18})$$

Funding. Institute of Information & Communications Technology Planning & Evaluation (IITP) grant funded by the Korea government (MSIT) (No. 2020-0-00914, Development of hologram printing downsizing technology based on holographic optical element(HOE)).

Acknowledgments. Hwi Kim* and Joonku Hahn** are the corresponding author and co-corresponding author, respectively.

Disclosures. The authors declare no conflicts of interest.

Data availability. Data underlying the results presented in this paper are not publicly available at this time but may be obtained from the authors upon reasonable request.

References

1. R. Häussler, Y. Gritsai, E. Zschau, R. Missbach, H. Sahn, M. Stock, and H. Stolle, "Large real-time holographic 3D displays: enabling components and results," *Appl. Opt.* **56**(13), F45–F52 (2017).
2. S. Reichelt, R. Häussler, G. Fütterer, N. Leister, H. Kato, N. Usukura, and Y. Kanbayashi, "Full-range, complex spatial light modulator for real-time holography," *Opt. Lett.* **37**(11), 1955–1957 (2012).
3. J. H. Choi, J. -H. Yang, J. -E. Pi, C. -Y. Hwang, Y. -H. Kim, G. H. Kim, H. -O. Kim, and C. -S. Hwang, "The new route for realization of 1- μm -pixel-pitch high-resolution displays," *SID Int. Symp. Digest Tech. Papers* **50**(1), 319–321 (2019).
4. H. Takagi, K. Nakamura, T. Goto, P. B. Lim, and M. Inoue, "Magneto-optic spatial light modulator with submicron-size magnetic pixels for wide-viewing-angle holographic displays," *Opt. Lett.* **39**(11), 3344–3347 (2014).
5. Y. Takaki and K. Fujii, "Viewing-zone scanning holographic display using a MEMS spatial light modulator," *Opt. Express* **22**(20), 24713–24721 (2014).
6. S.-Y. Lee, H. N. Kim, Y. H. Kim, T. -Y. Kim, S. -M. Cho, H. B. Kang, and C.-S. Hwang, "Design method of tunable pixel with phase-change material for diffractive optical elements," *ETRI Journal* **39**(3), 390–397 (2017).
7. J. Liang, J. Kohn, M. F. Becker, and D. J. Heinzen, "High-precision laser beam shaping using a binary-amplitude spatial light modulator," *Appl. Opt.* **49**(8), 1323–1330 (2010).

8. S. Li, L. Ding, P. Du, Z. Lu, Y. Wang, L. Zhou, and X. Yan, "Using the spatial light modulator as a binary optical element: application to spatial beam shaping for high-power lasers," *Appl. Opt.* **57**(24), 7060–7064 (2018).
9. X. Li, L. Chen, Y. Li, X. Zhang, M. Pu, Z. Zhao, X. Ma, Y. Wang, M. Hong, and X. Luo, "Multicolor 3D meta-holography by broadband plasmonic modulation," *Sci. Adv.* **2**(11), e1601102 (2016).
10. Z. Huang, D. L. Marks, and D. R. Smith, "Out-of-plane computer-generated multicolor waveguide holography," *Optica* **6**(2), 119–124 (2019).
11. J. Hahn, H. Kim, Y. Lim, G. Park, and B. Lee, "Wide viewing angle dynamic holographic stereogram with a curved array of spatial light modulators," *Opt. Express* **16**(16), 12372–12386 (2008).
12. J. An, K. Won, Y. Kim, J.-Y. Hong, H. Kim, Y. Kim, H. Song, C. Choi, Y. Kim, J. Seo, A. Morozov, H. Park, S. Hong, S. Hwang, K. Kim, and H.-S. Lee, "Slim-panel holographic video display," *Nat. Comm.* **11**(1), 5568 (2020).
13. O. Kunieda and K. Matsushima, "High-quality full-parallax full-color three-dimensional image reconstructed by stacking large-scale computer-generated volume holograms," *Appl. Opt.* **58**(34), G104–G111 (2019).
14. J. W. Wu, Z. X. Cheng, and T. J. Cui, "Anisotropic metasurface holography in 3-D space with high resolution and efficiency," *IEEE Trans. Antennas Propag.* **69**(1), 302–316 (2021).
15. S. Hwang, J. Cho, S. Jeon, H.-J. Kang, Z.-J. Zhao, S. Park, Y. Lee, J. Lee, M. Kim, J. Hahn, B. Lee, J. Jeong, H. Kim, and J. R. Youn, "Gold-Nanocluster-Assisted Nanotransfer Printing Method for Metasurface hologram fabrication," *Sci. Rep.* **9**, 1–12 (2019).
16. G.-Y. Lee, J.-Y. Hong, S. Hwang, S. Moon, H. Kang, S. Jeon, H. Kim, J. Jeong, and B. Lee, "Metasurface eyepiece for augmented reality," *Nature Comm.* **9**, 4562 (2018).
17. G.-Y. Lee, G. Yoon, S.-Y. Lee, H. Yun, J. Cho, K. Lee, H. Kim, J. Rho, and B. Lee, "Complete amplitude and phase control of light using broadband holographic metasurfaces," *Nanoscale* **10**(9), 4237–4245 (2018).
18. Y. Tsuchiyama and K. Matsushima, "Full-color large-scaled computer-generated holograms using RGB color filters," *Opt. Express* **25**(3), 2016–2030 (2017).
19. S. Jiao, Z. Zhuang, and W. Zou, "Fast computer generated hologram calculation with a mini look-up table incorporated with radial symmetric interpolation," *Opt. Express* **25**(1), 112–123 (2017).
20. A. Symeonidou, D. Blinder, and P. Schelkens, "Colour computer-generated holography for point clouds utilizing the Phong illumination model," *Opt. Express* **26**(8), 10282–10298 (2018).
21. K. Matsushima and N. Sonobe, "Full-color digitized holography for large-scale holographic 3D imaging of physical and nonphysical objects," *Appl. Opt.* **57**, A150–A156 (2018).
22. D.-Y. Park and J.-H. Park, "Generation of distortion-free scaled holograms using light field data conversion," *Opt. Express* **29**(1), 487–508 (2021).
23. J.-H. Park, "Efficient calculation scheme for high pixel resolution non-hogel-based computer-generated hologram from light field," *Opt. Express* **28**(5), 6663–6683 (2020).
24. J. Roh, K. Kim, E. Moon, S. Kim, B. Yang, J. Hahn, and H. Kim, "Full-color holographic projection display system featuring an achromatic Fourier filter," *Opt. Express* **25**(13), 14774–14782 (2017).
25. S. Park, J. Roh, S. Kim, J. Park, H. Kang, J. Hahn, Y. Jeon, S.-W. Park, and H. Kim, "Characteristics of complex light modulation through an amplitude-phase double-layer spatial light modulator," *Opt. Express* **25**(4), 3469–3480 (2017).
26. Y. Zhao, L. Cao, H. Zhang, D. Kong, and G. Jin, "Accurate calculation of computer-generated holograms using angular-spectrum layer-oriented method," *Opt. Express* **23**(20), 25440–25449 (2015).
27. T. Senoh, Y. Ichihashi, R. Oi, H. Sasaki, and K. Yamamoto, "Study on a holographic TV system based on multiview images and depth maps," *Proc. SPIE* **8644**, 86440A (2013).
28. N. Takada, T. Shimobaba, H. Nakayama, A. Shiraki, N. Okada, M. Oikawa, N. Masuda, and T. Ito, "Fast high-resolution computer-generated hologram computation using multiple graphics processing unit cluster system," *Appl. Opt.* **51**(30), 7303–7307 (2012).
29. J.-S. Chen and D. P. Chu, "Improved layer-based method for rapid hologram generation and real-time interactive holographic display applications," *Opt. Express* **23**(14), 18143–18155 (2015).
30. L. Shi, B. Li, C. Kim, P. Kellnhofer, and W. Matusik, "Towards real-time photorealistic 3D holography with deep neural networks," *Nature* **591**(7849), 234–239 (2021).